Biosensors and Bioelectronics 142 (2019) 111525

Contents lists available at ScienceDirect

Biosensors and Bioelectronics

journal homepage: www.elsevier.com/locate/bios

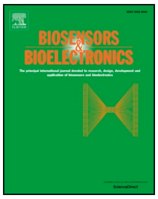

Amplified oxygen reduction signal at a Pt-Sn-modified TiO_2 nanocomposite on an electrochemical aptasensor

LeLe Li[a], Xiaoqiang Liu[a,*], Liwei Yang[a], Si Zhang[a], HeJie Zheng[a], Yunfei Tang[a], Danny K.Y. Wong[b,**]

[a] *Henan Joint International Research Laboratory of Environmental Pollution Control Materials, College of Chemistry and Chemical Engineering, Henan University, Kaifeng, Henan Province, 475004, PR China*

[b] *Department of Molecular Sciences, Macquarie University, Sydney, NSW, 2109, Australia*

ARTICLE INFO

Keywords:
Pt-Sn@TiO_2 composite
Oxygen reduction reaction
Electrochemical aptasensor
RecJ$_f$ exonuclease
Streptomycin

ABSTRACT

In this work, a metallic composite with strong electrocatalytic property was designed by uniformly decorating Pt and Sn nanoparticles on the surface of TiO_2 nanorods (Pt–Sn@TiO_2). A detection scheme was then developed based on a dual signal amplification strategy involving the Pt–Sn@TiO_2 composite and exonuclease assisted target recycling. The Pt–Sn@TiO_2 composite exhibited an enhanced oxygen reduction current owing to the synergistic effect between Pt and Sn, as well as high exposure of Pt (111) crystal face. Initially, a Pt–Sn@TiO_2 modified glassy carbon electrode produced an amplified electrochemical signal for the reduction of dissolved oxygen in the analyte solution. Next, a DNA with a complementary sequence to a streptomycin aptamer (cDNA) was immobilised on the Pt–Sn@TiO_2 modified electrode, followed by the streptomycin aptamer that hybridised with cDNA. The corresponding oxygen reduction current was diminished by 51% attributable to the hindrance from the biomolecules. After a mixture of streptomycin and RecJ$_f$ exonuclease was introduced, both the streptomycin-aptamer complex and the cDNA were cleaved from the electrode, making the Pt–Sn and Pt (111) surface available for oxygen reduction. RecJ$_f$ would also release streptomycin from the streptomycin-aptamer complex, allowing it to complex again with aptamers on the electrode. This has then promoted a cyclic amplification of the oxygen reduction current by 85%, which is quantitatively related to streptomycin. Under optimal conditions, the aptasensor exhibited a linear range of 0.05–1500 nM and a limit of detection of 0.02 ± 0.0045 nM streptomycin. The sensor was then used in the real-life sample detection of streptomycin to demonstrate its potential applications to bioanalysis.

1. Introduction

As a fast-growing analytical tool, electrochemical aptasensors have demonstrated several advantages including excellent selectivity, low cost, facile detection procedure, and rapid response for specific analytes (Golub et al., 2009; Tavakkoli et al., 2019; Wang et al., 2018a; Yang et al., 2017). In particular, aptamers are superior over the more conventional biorecognition element of antibody due to their low cost, mass production, ease of synthesis and modification, short detection time, excellent thermal stability and inherent binding affinity (Chen et al., 2018; Liu et al., 2017a, 2018; Tang et al., 2018a; Urbanová et al., 2018). For example, an aptamer for the antibiotic streptomycin was immobilised on a gold nanoparticle-thiol graphene quantum dot nanocomposite to construct an ultrasensitive streptomycin aptasensor (Ghanbari and Roushani, 2018). Based on an increasing electrochemical impedance of the sensor arising from the presence of an aptamer-streptomycin complex on its surface, the aptasensor was characterised by a linear range from 0.1 to 700 $pg\,mL^{-1}$ and a detection limit of 0.033 $pg\ mL^{-1}$ of streptomycin in human serum samples. Another example of an aptasensor was based on a TiO_2–$BiVO_4$ heterostructural support for cross-linking a DNA aptamer for sensitive detection of 17β-estradiol (Liu et al., 2017a). The TiO_2 nanospheres provided a biocompatible microenvironment to enhance the loading of aptamer molecules. In this way, the aptasensor was demonstrated to exhibit a linear range from 0.1 to 250 pM and a detection limit of 0.022 pM of 17β-estradiol in human urine samples. An electrochemical aptasensor was also developed by combining specific DNA aptamers with a MoS_2–TiO_2@Au composite for the detection of tetracycline (Tang et al.,

---

[*] Corresponding author.
[**] Corresponding author.
E-mail addresses: liuxq@henu.edu.cn (X. Liu), Danny.Wong@mq.edu.au (D.K.Y. Wong).

https://doi.org/10.1016/j.bios.2019.111525
Received 17 May 2019; Received in revised form 16 July 2019; Accepted 18 July 2019

2018b). In this strategy, a tetracycline aptamer was hybridised with its complementary biotin-DNA oligonucleotide, followed by avidin-horseradish peroxidase. Hence, a horseradish peroxidase catalysed reduction of H_2O_2 was promoted to produce an amplified electrochemical response. The presence of increasing tetracycline concentration hindered the binding of the biotin-DNA oligonucleotide to the aptamer, leading to a diminishing electrochemical H_2O_2 reduction signal, which was then quantitatively related to tetracycline. This aptasensor showed a linear range from 0.15 to 600 nM, and a detection limit of 0.05 nM tetracycline in milk samples.

In recent years, several nanomaterials with strong catalytic property were designed for signal amplification in DNA hybridisation to improve the analytical detection capability of aptasensors (Chen et al., 2015; Dong et al., 2017; Zhang et al., 2017; Zheng et al., 2014). For example, metallic nanoparticles, carbon based nanomaterials, magnetic nanoparticles and quantum dots have been extensively applied to many sensor designs including aptasensors because of their unique electrochemical, catalytic, mechanical and optical properties, which were exploited to enhance analytical detection sensitivity and specificity (Evtugyn et al., 2014; Sai-Anand et al., 2018). For example, a bisphenol A aptasensor was developed by electrodepositing the bimetallic alloy of Au–Pt nanoparticles on a carboxylated carbon nanotube-modified glassy carbon electrode. By monitoring differential pulse voltammetric responses of acriflavine as a redox probe, this aptasensor exhibited two linear ranges from 0.1 to 1.0 pM and 10–700 pM, and a detection limit of 0.035 pM of bisphenol A in water samples (Beiranvand et al., 2017). Owing to poor stability, high cost and scarcity of Pt electrocatalysts (Wang et al., 2018b), Pt-based bimetallic alloys, instead of Pt alone, were increasingly used not only to reduce the consumption of Pt, but also to improve the catalytic activity by exploiting the synergistic effect between two metals (Liu et al., 2013). For example, Pt–Ag nanotubes composed of surface Pt_5Ag_3 and the face-centred cube of PtAg alloy (111) exhibited an extraordinary oxygen reduction reaction activity with a specific activity of 1.13 mA cm^{-2} and a mass activity of 0.688 A mg^{-1} Pt at 0.9 V, which are respectively 4.5 times and 4.3 times higher than those of commercial Pt/C catalysts (Zhang et al., 2018). These results were attributed to the porous and rough surface of PtAg nanotubes with a large surface area, which offered more reaction sites and thus enhanced activity.

The performance of electrocatalysts is also significantly affected by their support that provides a porous, large and stable surface to load the electrocatalysts (Cho et al., 2014; Deng et al., 2019; Maass et al., 2008; Ozdokur et al., 2016). However, conventional carbon-based nanomaterial supports may not simultaneously offer all these features. For example, an unstable electrocatalyst support may cause Pt to detach from the support, leading to a loss of electrocatalyst activity (Khotseng et al., 2016; Sui et al., 2017). Recently, TiO_2 nanomaterials have been increasingly used as biosensor scaffolds for immobilising biomolecules due to their porous structure, large surface area, remarkable stability and strong capability to retain biomolecule activity (Huo et al., 2016; Liu et al., 2017b). Therefore, they are potentially ideal supports for electrocatalysts and subsequently applied to biosensor development (Antolini et al., 2006; Cao et al., 2015).

The present work is aimed at developing a bimetallic Pt–Sn on TiO_2 nanocomposite with highly efficient electrocatalytic property towards oxygen reduction reaction and applying it to the development of a sensitive aptasensor. A significant aspect of this design lies in the use of a bimetallic Pt–Sn alloy that is resistant to oxidation, coupled with a TiO_2 support to provide high stability for the sensing platform. In addition, we have developed an ultrasensitive detection strategy, using streptomycin as a model analyte, based on a dual signal amplification system composed of a Pt–Sn@TiO_2 ternary composite and exonuclease assisted target recycling. By alloying Sn with Pt, the electrons in the 5d orbital of a Pt atom may be promoted to the corresponding orbital of Sn, increasing the electron vacancy on the Pt atom. The interaction of the vacancy in the Pt atom with π orbital electrons of O_2 will then favour the adsorption of molecular oxygen on the Pt surface to form a strong Pt–O_2 coordination bond. In this way, the density of bonding electrons between O–O was reduced, resulting in lower bond energy. In other words, the formation of Pt–O_2 bond facilitates the cleavage of O–O bond (Bai et al., 2011; Beyhan et al., 2015; Khotseng et al., 2016). In terms of oxygen reduction reaction, there are two reaction pathways, (i) a direct pathway involving a 4-electron reaction to produce water ($O{=}O + 4e^- + 4H^+ \rightarrow 2H_2O$), and (ii) a continuous reaction pathway in which an H_2O_2 intermediate is firstly produced and then the H_2O_2 undergoes a 2-electron reduction to produce water ($O{=}O + 2e^- + 2H^+ \rightarrow H{-}O{-}O{-}H$; $H{-}O{-}O{-}H + 2e^- + 2H^+ \rightarrow 2H_2O$). In both reaction pathways, the dissociation of the O–O bond in O_2 determines the catalytic reduction rate. Therefore, the promotion of O–O bond cleavage will increase the catalytic oxygen reduction rate.

Notably, exonucleases are known to catalyse the hydrolysis of a phosphodiester bond between adjacent oligonucleotides to produce mononucleotides (Chen et al., 2016; Miao et al., 2016). In particular, according to Chen et al. (2017), $RecJ_f$ exonuclease is expected to selectively cleave the streptomycin-aptamer complex by converting the aptamer to a mononucleotide and liberate streptomycin, which will allow streptomycin to further complex with a remaining aptamer on the electrode surface. In this way, streptomycin is repeatedly released by $RecJ_f$ exonuclease, giving rise to a multiple-signal amplification for the electrochemical oxygen reduction signal. In addition, $RecJ_f$ exonuclease was reportedly able to also cleave single-strand DNA (Chen et al., 2016).

Scheme 1 illustrates the steps adopted in developing our sensor. Initially, TiO_2 nanorods will be used as a support for loading Pt–Sn nanoparticles to construct a ternary electrocatalyst, denoted as a Pt–Sn@TiO_2 nanocomposite, before it is secured on a glassy carbon electrode. As noted above, the interaction between Pt and Sn, as well as high availability of Pt (111), will catalyse the reduction of dissolved oxygen in an analyte solution. In the next step, a DNA with a complementary sequence to a streptomycin aptamer (cDNA) is immobilised on the electrode, followed by a streptomycin aptamer that hybridises with cDNA to obtain an electrochemical streptomycin aptasensor. In this way, the immobilised aptamer–c-DNA structure on the electrode will hinder the oxygen reduction reaction. As noted above, by introducing a streptomycin–$RecJ_f$ exonuclease mixture, both the streptomycin-aptamer complex and cDNA are cleaved by $RecJ_f$ from the electrode surface, which then facilitates an enhanced oxygen reduction reaction. Therefore, the oxygen reduction current is expected to be quantitatively related to streptomycin. This electrochemical aptasensor will then be demonstrated to exhibit high specificity, sensitivity, stability and low detection limit for the detection of streptomycin.

2. Materials and methods

2.1. Material and reagents

Analytical grade reagents were used as received without further purification. Chloroform, ethylene glycol and absolute ethanol were purchased from Sinopharm Chemical Reagent Co. Ltd, China. Titanium tetrachloride was acquired from Tianjin Chemical Reagent Co. Ltd., China. K_2PtCl_6 was purchased from Nine-Dinn Chemistry (Shanghai) Co. Ltd., China, while $SnCl_2{\cdot}2H_2O$ was from Alfa Aesar (China) Chemical Co. Ltd. Bis(sulfo-succinimidyl) suberate sodium salt, bovine serum albumin (BSA), and chitosan (85% deacetylation) were all acquired from Sigma-Aldrich Chemical Co. (St. Louis, MO, USA). $RecJ_f$ exonuclease was purchased from New England Biolabs, Inc. (U.K.), and streptomycin was from Aladdin Reagent Co. Ltd., Shanghai, China. Ultrapure water ($\geq 18\,M\Omega\ cm^{-1}$) obtained from a Millipore water purification system was employed in all assays. Phosphate buffered saline (PBS, pH 7.4) was prepared by mixing 0.1 M KH_2PO_4, 0.1 M

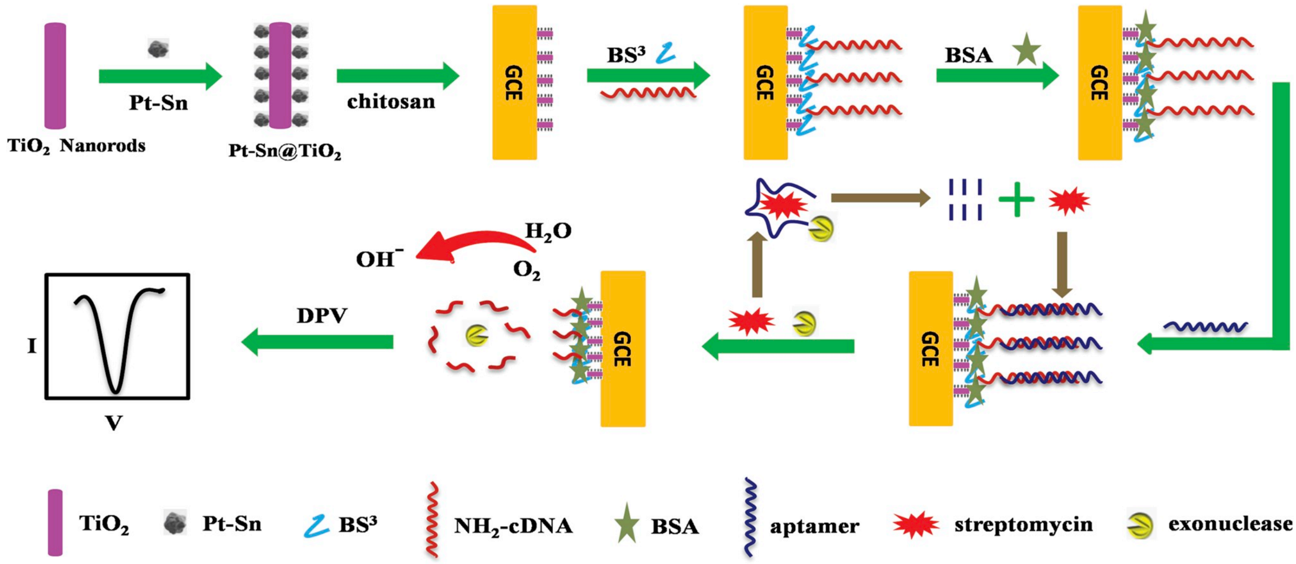

Scheme 1. Schematic diagram of the assembly of the streptomycin aptasensor. “GCE” denotes glassy carbon electrode and “BS^3” denotes bis(sulfo-succinimidyl) suberate sodium salt.

K_2HPO_4, and 0.1 M KCl. The streptomycin aptamer and its complementary DNA with the following sequences were purchased from Shanghai Sangon Biotechnology Co. Ltd., Shanghai, China:

Streptomycin aptamer: 5'-TTT TAG GGA ATT CGT CGA CGG ATC CGG GGT CTG GTG TTC TGC TTT GTT CTG TCG GGT CGT CTG CAG GTC GAC GCA TGC GCC G-3'

Complimentary strand (cDNA): 5'-GGT GTT GTT AGC GGC GTA ACG AAT TCC CTA-NH_2-3'

Note that only the last 10 nucleotides of 3′-end of cDNA bind to the last 10 nucleotides of 5′-end of streptomycin aptamer through base pairings. Underlined bases in blue were added at the 5′ end of the streptomycin aptamer to facilitate the recognition of the single strand structure in aptamer-streptomycin conjugates by $RecJ_f$ exonuclease.

2.2. Apparatus

All electrochemical measurements were performed on a CHI630D electrochemical workstation (CH Instruments, Shanghai, China) in a three-electrode cell consisting of a Ag|AgCl (3.0 M KCl) reference electrode, a platinum wire counter electrode, and a Pt–Sn@TiO_2 modified glassy carbon working electrode. Electrochemical impedance spectroscopy was conducted on an IM6ex electrochemical station (ZAHNER, Germany). The appearance and chemical composition of the prepared materials were characterised by scanning electron microscopy (JSM-7500F, JEOL, Japan), energy dispersive X-ray (JSM-7500F, JEOL, Japan), transmission electron microscopy (Tecnai G2 20, USA), and X-ray diffraction (XRD, Bruker D8 Advance, Germany) with a Cu Kα radiation ($\lambda = 1.5406$ nm). Elemental composition and valance state of the prepared materials were also studied using X-ray photoelectron spectroscopy (ESCALAB 250Xi, USA) with a monochromated Al Kα source ($h\nu = 1486.6$ eV, 150 W power and 500 µm beam spot). The obtained spectra were calibrated using the C1s peak (284.8 eV) and analysed by XPSPEAK41 software.

2.3. Preparation of cylindrical TiO_2 nanorods

Cylindrical TiO_2 nanorods were synthesised using a modified hydrothermal method (Yang et al., 2015). Initially, 0.9 mL titanium tetrachloride was slowly added to a beaker containing 9.5 mL ultrapure water in an ice-water bath (0–5°C). After vigorously stirring the mixture for 30 min, a white suspension was obtained. In the next step, 0.9 mL chloroform was added to the above white suspension, which was stirred for another 30 min, before it was transferred to a 50-mL Teflon-lined stainless steel autoclave. The autoclave was placed in an oven maintained at 160°C for 12 h. The obtained product was collected, washed carefully with deionised water and absolute ethanol until the pH reached ~7.0, and then dried in a vacuum at 60°C overnight.

2.4. Fabrication of a Pt–Sn@TiO_2 composite

A Pt–Sn@TiO_2 composite was synthesised by an alcohol-reduction reaction. Initially, 0.19 g of K_2PtCl_6 and 0.044 g of $SnCl_2{\cdot}2H_2O$ were dissolved in 100 mL of ethylene glycol, and the solution pH was adjusted to 12 with 2 M NaOH in ethylene glycol. This was followed by the addition of 0.4 g of cylinder-shaped TiO_2 nanorods to the above solution to obtain a mixture solution, which was sonicated for 5 min and then refluxed at 160°C under N_2 gas for 3 h. Finally, the mixture was cooled to room temperature with stirring, and the powder was collected, filtered, washed with absolute ethanol and dried in a vacuum at 60°C for 24 h.

2.5. Fabrication of streptomysin aptasensor

In fabricating the streptomysin aptasensor, 2 mg of Pt–Sn@TiO_2 nanocomposite was initially dispersed in 1 mL of 0.2% chitosan solution (in 1% w/v acetic acid), which was sonicated for 30 min to obtain a homogeneous suspension. Next, 5 µL of the above suspension was applied to the pre-treated glassy carbon electrode and dried at room temperature. Then, 5 µL of a 2 mg mL^{-1} bis(sulfo-succinimidyl) suberate sodium salt solution was delivered to the modified glassy carbon electrode and left at ambient temperature for 1 h. Subsequently, 5 µL of aminated complementary DNA (NH_2-cDNA, 2 µM) of streptomycin aptamer was immobilised on the modified glassy carbon electrode and incubated at 4°C overnight. After rinsing with PBS to remove unbound NH_2-cDNA, the electrode was incubated with 5 μL of 3% (w/v) bovine serum albumin for 1 h to block the active sites of non-specific binding. Finally, the electrode was thoroughly rinsed with PBS and incubated with 5 L of streptomycin aptamer for 1 h at 37°C to promote the hybridisation of cDNA with streptomycin aptamer. After careful rinsing with PBS, the obtained aptasensor was incubated in 5 L of increasing concentrations of streptomycin solution including 20 U $RecJ_f$ exonuclease at 37°C for 1.5 h. Finally, the aptasensor was rinsed with PBS and stored at 4°C for subsequent use.

3. Results and discussion

In this paper, a highly efficient electrocatalyst of Pt–Sn@TiO_2 was synthesised and used as a scaffold for the development of an electrochemical aptasensor. As described above, we have used a Pt–Sn@TiO_2 nanocomposite to accommodate a streptomycin aptamer with an aminated complementary DNA sequence. In the presence of streptomycin and $RecJ_f$ exonuclease, both the aptamer and cDNA were cleaved from the electrode surface, subjecting the Pt–Sn@TiO_2 nanocomposite to dissolved oxygen in solution and hence the electrocatalytic oxygen reduction reaction. The measured oxygen reduction peak current was therefore enhanced to provide a sensitive and specific streptomycin detection strategy. In the following sections, each component of the aptasensor was carefully characterised by microscopic, spectroscopic and electrochemical techniques.

3.1. Morphological and compositional characterisations of nanomaterials

The size and morphology of TiO_2 nanorods and Pt–Sn@TiO_2 nanocomposites were characterised by scanning electron microscopy and transmission electron microscopy. The scanning electron micrograph (left panel) and the transmission electron micrograph (right panel) in Fig. 1A show that the as-prepared TiO_2 nanomaterial possessed a cylinder-shaped nanostructure with smooth surface. An average diameter of ~20 nm and an axial length of ~180 nm were estimated from the figure. However, as shown in the scanning electron micrograph in Fig. 1B, many tiny prominences are observable on the surface of Pt–Sn@TiO_2 nanocomposites, making the surface appear to be much rougher than that of TiO_2 nanorods. We ascribed the prominences to the successful deposition of Pt–Sn alloy nanoparticles on TiO_2 nanorods. The transmission electron micrograph of Pt–Sn@TiO_2 nanocomposites in Fig. 1C displayed many small and dark nanoparticle dots on the TiO_2 nanorod surface. We used this as a supporting evidence for

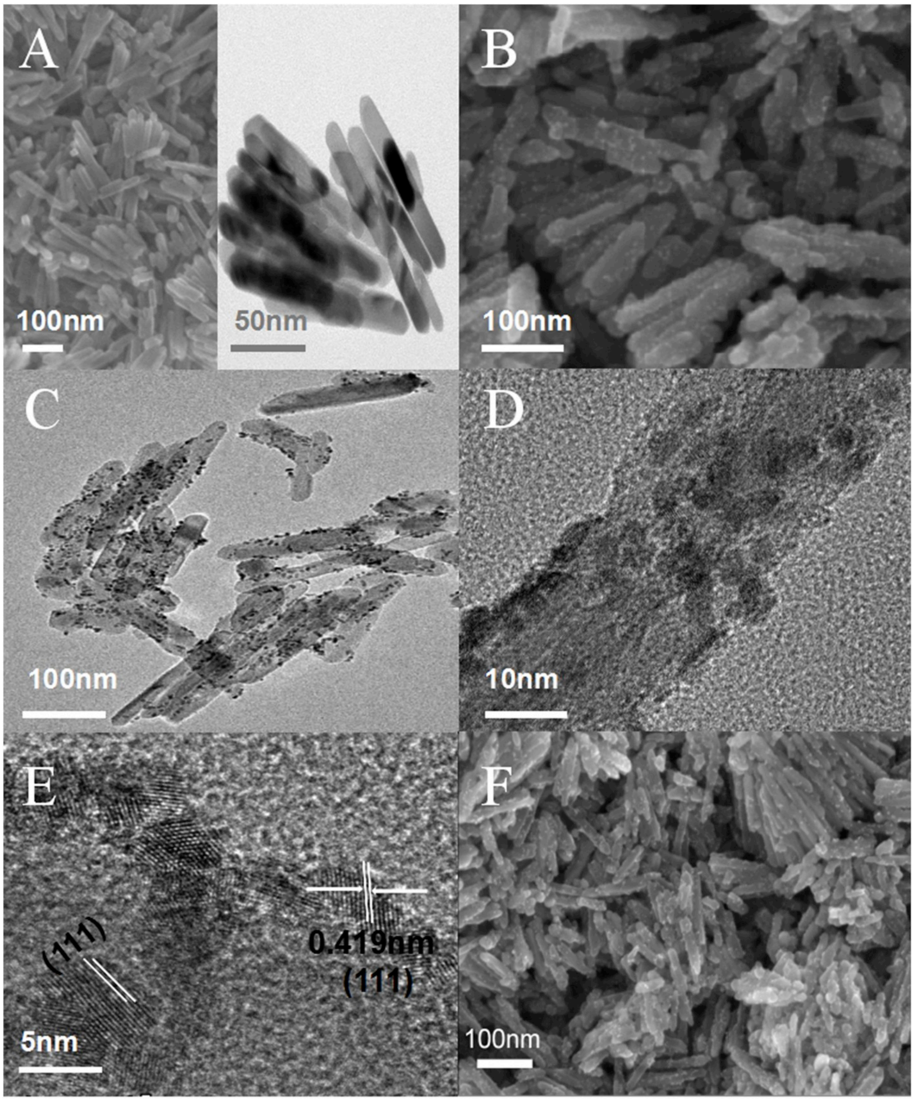

Fig. 1. (A) Scanning electron micrograph (left panel) and transmission electron micrograph (right panel) of cylinder-shaped TiO_2 nanorods, (B) scanning electron micrograph and (C) transmission electron micrograph of Pt–Sn@TiO_2 composite, (D) and (E) high-resolution transmission electron micrographs of Pt–Sn@TiO_2 composite at 10 × and 50 × magnifications, (F) scanning electron micrograph of a Pt–Sn@TiO_2 nanocomposite modified biosensor.

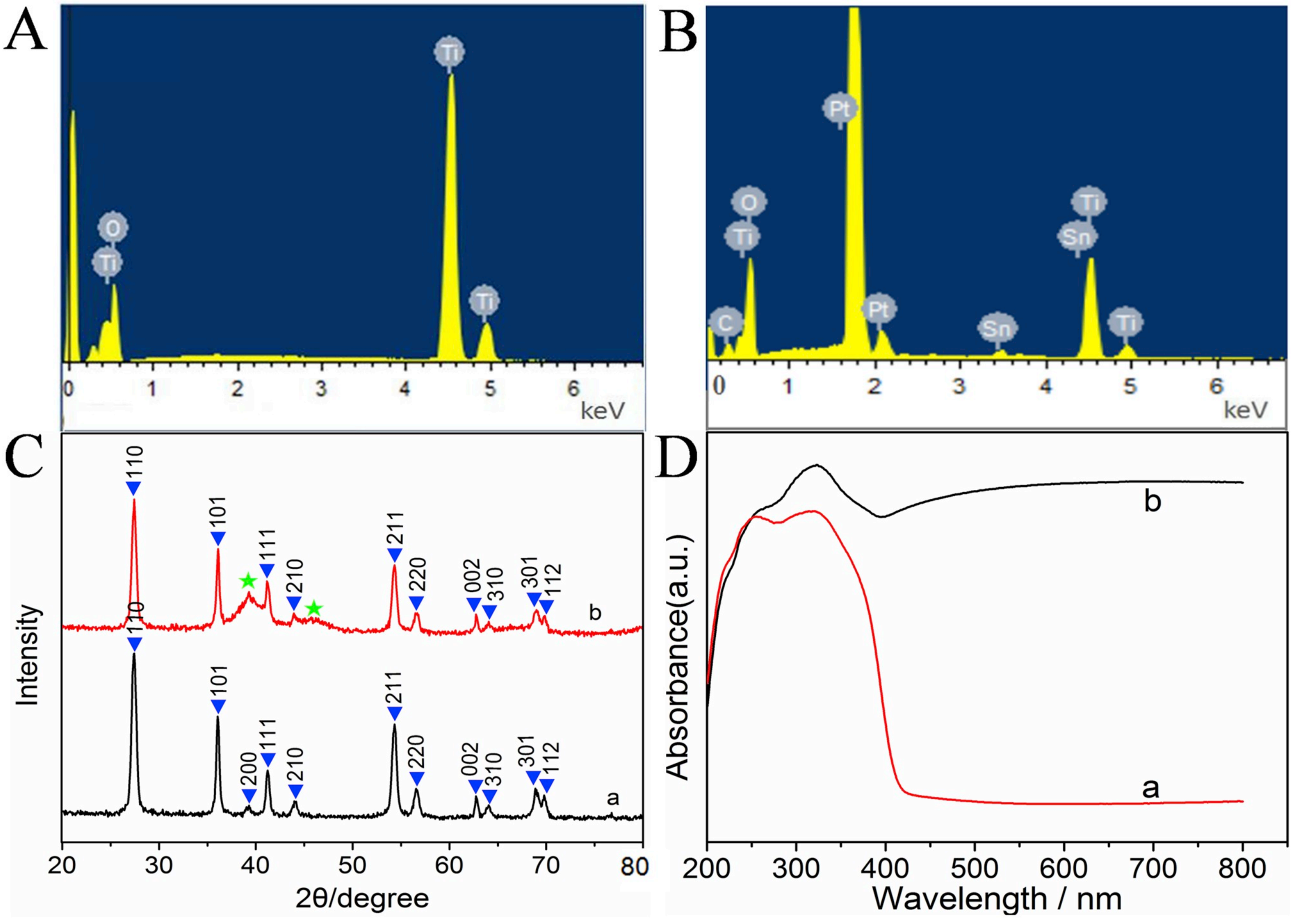

Fig. 2. Energy dispersive X-ray patterns of (A) TiO_2 nanorods and (B) Pt–Sn@TiO_2 composite; (C) XRD patterns of (a) TiO_2 and (b) Pt–Sn@TiO_2 composite; (D) UV-vis diffuse reflectance spectra of (a) rutile TiO_2 and (b) Pt–Sn@TiO_2 composite.

the formation of a ternary composite. In the 10 × magnified micrograph of Pt–Sn@TiO_2 in Fig. 1D, the spherical morphology of the ternary composites is clearly visible and their average diameter was estimated to be ~5 nm. The lattice structure of the Pt–Sn alloy was further revealed by high-resolution transmission electron microscopy. The 50 × magnified micrograph of Pt–Sn@TiO_2 is displayed in Fig. 1E, on which the lattice spacing of the face-centred cubic (111) plane for a Pt–Sn alloy was estimated to be 0.42 nm. This result is in agreement with ~0.419 nm reported by Zhang et al. for the lattice spacing of the face-centred cubic (111) plane for a Pt–Sn alloy (Zhang et al., 2017, 2018). This is again an indication of a successful synthesis of Pt–Sn@TiO_2 nanocomposites. The morphology of a Pt–Sn@TiO_2 nanocomposite modified biosensor was also characterised by scanning electron microscopy. As shown in Fig. 1F, an aptamer|BSA|cDNA|Pt–Sn@TiO_2|glassy carbon electrode displayed a rough surface consisting of cylinder-shaped nanostructures with an average diameter of ~20 nm and an axial length of ~180 nm. This scanning electron micrograph demonstrated a dense coverage of Pt–Sn@TiO_2 composites on the sensor surface, which provides a large specific surface area for considerable loading of biomolecules.

The elemental composition of the prepared TiO_2 and Pt–Sn@TiO_2 was investigated by energy dispersive X-ray analysis and the results obtained are shown in Fig. 2. In Fig. 2A, several peaks in the spectrum of the TiO_2 were assigned to Ti and O peaks after comparing their peak positions with those reported in Liu et al.'s work involving the assembly of a MoS_2 nanosheet-TiO_2 nanorod heterostructure as a sensor scaffold for photoelectrochemical biosensing (Liu et al., 2017c). In Fig. 2B, Ti, O, Pt, Sn, and C elemental peaks were clearly identified in the energy dispersive X-ray pattern of the Pt–Sn@TiO_2 composite, as suggested by Zhang et al.'s work on fabricating Pt/Sn–In_2O_3 nanoflowers with advanced oxygen reduction reaction performance for high-sensitivity microRNA electrochemical detection (Zhang et al., 2017). The appearance of distinct peaks attributed to Pt and Sn implied Pt–Sn alloy nanoparticles were successfully modified on the TiO_2 surface.

3.2. X-ray diffraction and UV-visible spectroscopy of prepared nanomaterials

The crystalline structures of the as-prepared TiO_2 and Pt–Sn@TiO_2 were analysed by X-ray diffraction. The X-ray diffraction pattern of TiO_2 depicted in Fig. 2C shows a series of characteristic diffraction peaks at 27.44°, 36.04°, 39.29°, 41.22°, 43.98°, 54.33°, 56.55°, 62.75°, 64.01°, 68.88° and 69.84° (trace a), corresponding to the (110), (101), (200), (111), (210), (211), (220), (002), (310), (301) and (112) crystal faces of rutile TiO_2 (Liu et al., 2017c). Moreover, these characteristic peaks of TiO_2 are all sharp with an intense magnitude, and no other impurity peaks were observed, indicating the successful synthesis of high purity rutile TiO_2. The X-ray diffraction spectrum of Pt–Sn@TiO_2 composite (trace b) exhibit almost all the characteristic peaks ascribed to TiO_2 alone (trace a) and two other distinct characteristic peaks at 39.23° and 45.73° indexed to the (111) and (200) crystal planes of Pt–Sn alloy (Khotseng et al., 2016), which supported the successful deposition of Pt–Sn alloy nanoparticles on TiO_2 to form a ternary composite. Furthermore, the peak intensity of TiO_2 in Pt–Sn@TiO_2 composite (trace b) is ~20% weaker than that in TiO_2 alone (trace a), which may be attributed to the coverage of TiO_2 surface by Pt–Sn alloy nanoparticles. These results are consistent with those obtained in microscopic analysis, indicating the successful preparation of the Pt–Sn@TiO_2 composite.

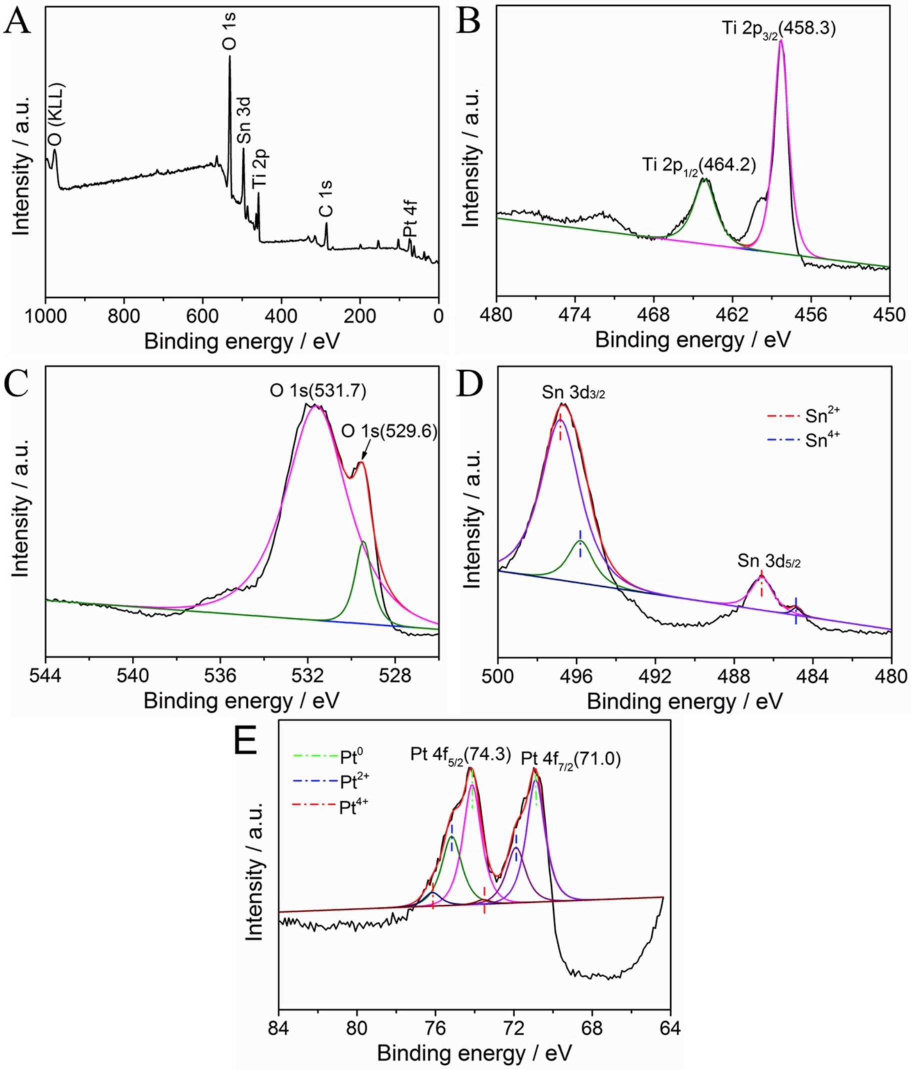

Fig. 3. X-ray photoelectron analysis of Pt–Sn@TiO_2 composite: (A) survey scan, and high-resolution spectra of (B) Ti 2p, (C) O 1 s, (D) Sn 3d and (E) Pt 4f.

As an effective complementary technique to X-ray diffraction, UV-visible diffuse reflectance spectrometry was performed to evaluate the optical absorption properties of TiO_2 and Pt–Sn@TiO_2 nanocomposites and the results obtained are displayed in Fig. 2D. In trace a of this figure, rutile TiO_2 nanorods showed an absorption edge at 420 nm, which, according to the Scherer equation (Liu et al., 2017a) ($\lambda = 1240 / E_g$, where λ is the absorption edge wavelength and E_g is the absorption edge wavelength), yielded an E_g of ~3.0 eV. Compared to the spectrum of TiO_2 nanorods alone in trace b, the prepared Pt–Sn@TiO_2 nanocomposite displayed strong absorption in both UV and visible regions ascribed to the bimetallic Pt–Sn nanoparticles, which significantly improved the visible light absorption of TiO_2.

3.3. *X-ray photoelectron spectroscopic characterisation of as-prepared Pt–Sn@TiO_2*

The surface chemical composition and valence status of the Pt–Sn@TiO_2 nanomaterial were investigated by X-ray photoelectron spectroscopic analysis. Fig. 3A shows a typical overall X-ray photoelectron spectroscopic survey spectrum that indicates the presence of Ti, O, Pt, Sn and C on the ternary composite surface. More specifically, the high-resolution spectrum of Ti 2p in Pt–Sn@TiO_2 in Fig. 3B was deconvoluted into one doublet at 458.3 and 464.2 eV, corresponding to the binding energy of Ti^{4+} $2p_{3/2}$ and Ti^{4+} $2p_{1/2}$, respectively, after comparing them to the two peaks at 458.4 eV and 464.1 eV in Zhao et al.'s work involving the fabrication of defective TiO_2 nanorods for investigating the effect of defects on photocatalytic activity of rutile TiO_2 nanorods (Zhao et al., 2015). The O 1s X-ray photoelectron spectrum in Fig. 3C presents distinct characteristic peaks at 529.6 and 531.7 eV (compared to 530.0 eV and 531.8 eV in Wang et al.'s work involving facile synthesis of nitrogen self-doped rutile TiO_2 nanorods (Wang et al., 2012)), which were attributed to the lattice oxygen [$Ti–O_6$] in TiO_2 and Ti–OH groups on the surface of TiO_2, respectively, indicating that the existence state of O was O^{2-} in the composite. As shown in Fig. 3D, the Sn 3d high resolution spectrum of Pt–Sn@TiO_2 composite was deconvoluted into two doublets of [Sn 1 (484.9 eV), Sn 2 (486.6 eV)] and [Sn 3 (495.8 eV), Sn 4 (496.9 eV)], which were assigned to Sn $3d_{5/2}$ and Sn $3d_{3/2}$, respectively, as suggested by Zhang et al.'s work on fabricating Pt/Sn–In_2O_3 nanoflowers with advanced oxygen reduction reaction performance for high-sensitivity microRNA electrochemical detection (Zhang et al., 2017). The Pt 4f X-ray photoelectron spectrum in Fig. 3E presents characteristic peaks of Pt $4f_{7/2}$ and Pt $4f_{5/2}$ located at 71.0 and 74.3 eV, which were deconvoluted to Pt^0, Pt^{2+} and Pt^{4+} states at the corresponding binding energies of 71.6 eV and 74.9 eV, 72.3 eV and 75.6 eV and 74.1 eV and 77.3 eV (Wang et al., 2010). In summary, we concluded that Pt–Sn@TiO_2 composite was successfully prepared based on the composition and elemental valence states obtained by the above X-ray photoelectron spectra.

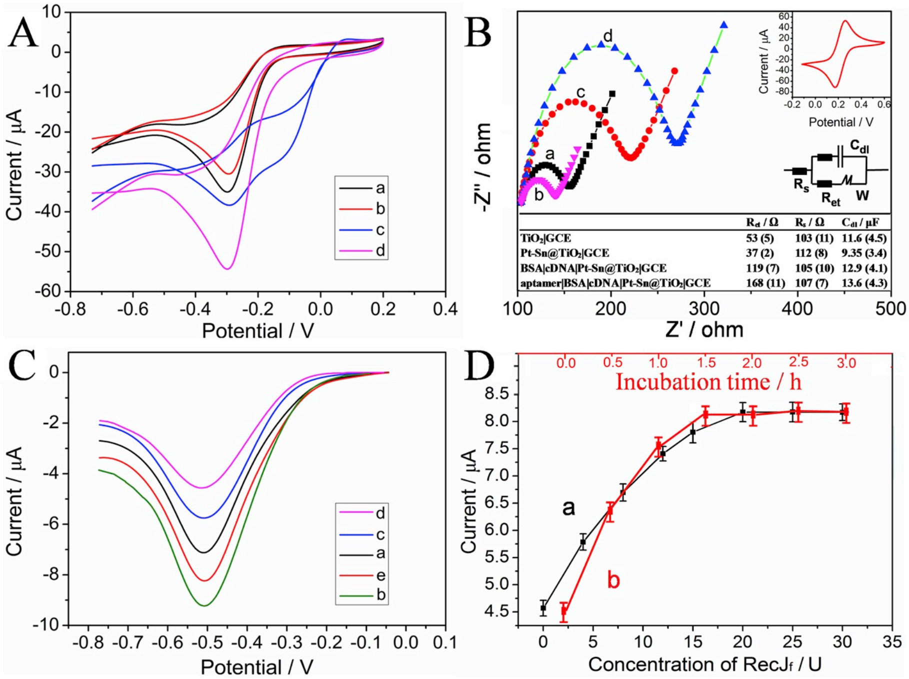

	R_{et} / Ω	R_s / Ω	C_{dl} / µF
TiO_2|GCE	53 (5)	103 (11)	11.6 (4.5)
Pt-Sn@TiO_2|GCE	37 (2)	112 (8)	9.35 (3.4)
BSA|cDNA|Pt-Sn@TiO_2|GCE	119 (7)	105 (10)	12.9 (4.1)
aptamer|BSA|cDNA|Pt-Sn@TiO_2|GCE	168 (11)	107 (7)	13.6 (4.3)

Fig. 4. (A) Cyclic voltammetric response of saturated oxygen at (a) a bare GCE, (b) a TiO_2|GCE, (c) a Pt@TiO_2|GCE and (d) a Pt–Sn@TiO_2|GCE in 0.1 M KOH; (B) electrochemical impedance spectra of 5 mM $[Fe(CN)_6]^{3-}$ and 5 mM $[Fe(CN)_6]^{4-}$ at (a) a TiO_2|GCE, (b) a Pt–Sn@TiO_2|GCE, (c) a BSA|cDNA|Pt–Sn@TiO_2|GCE and (d) an aptamer|BSA|cDNA|Pt–Sn@TiO_2|GCE in 0.1 M KCl; top right inset: cyclic voltammogram of 5 mM $[Fe(CN)_6]^{3-/4-}$ at aptamer|BSA|cDNA|Pt–Sn@TiO_2|GCE in 0.1M KCl; middle right inset: Randles equivalent circuit used in obtaining simulated impedance results shown in the bottom panel, (C) differential pulse voltammetric response of saturated O_2 at (a) a TiO_2|GCE, (b) a Pt–Sn@TiO_2|GCE, (c) a BSA|cDNA|Pt–Sn@TiO_2|GCE, (d) an aptamer|BSA|cDNA|Pt–Sn@TiO_2|GCE and (e) after incubation with 5 µL of 1.5 µM streptomycin containing 20 U $RecJ_f$ exonuclease in 0.1 M PBS (pH 7.4); (D) Effects of (a) $RecJ_f$ exonuclease concentration and (b) enzymatic reaction time.

3.4. Electrochemical characterisation of Pt–Sn@TiO_2

The catalytic property of Pt–Sn@TiO_2 was investigated by cyclic voltammetry of 30 mL O_2-saturated 0.1 M KOH electrolyte. In Fig. 4A, trace a shows a peak at ~-0.29 V corresponding to the reduction of O_2 to OH^- at a glassy carbon electrode. In trace b, a reduction peak is still observed at the TiO_2 modified glassy carbon electrode. However, a ~13% lower current in trace b relative to trace a is attributed to the limited electronic conductivity of semiconductor TiO_2. Notably, TiO_2 was used in this work to improve the stability and loading of the catalyst. In trace c, the Pt@TiO_2 catalyst modified glassy carbon electrode shows weak electrocatalytic activity toward oxygen reduction reaction. In contrast to Pt@TiO_2, the Pt–Sn@TiO_2 modified glassy carbon electrode enhanced the catalytic activity toward oxygen reduction reaction by ~41.7%, which most likely arose from the synergistic electronic effect between Pt and Sn coupling with a high composition of Pt (111) facets on the oxygen reduction reaction activity discussed under Introduction.

3.5. Characterisations of electrochemical aptasensor

In this work, electrochemical impedance spectroscopy of 5.0 mM $[Fe(CN)_6]^{3-}$ and 5.0 mM $[Fe(CN)_6]^{4-}$ in 0.1 M KCl was also used to investigate the fabrication procedure of the streptomycin aptasensor. As shown in Fig. 4B, Nyquist plots (imaginary impedance (Z”) versus real impedance (Z’) plots) for different nanomaterial modified electrodes were recorded over a 100 kHz–100 mHz frequency range at a DC potential of 0.23 V, superimposed by a 5 mV peak-to-peak AC potential. As shown by the top right inset of Fig. 4B, the DC potential of 0.23 V corresponds to the halfwave potential of the cyclic voltammogram of $[Fe(CN)_6]^{3-/4-}$ at the modified electrodes. Meanwhile, the middle right inset of Fig. 4B displays an equivalent circuit consisting of a solution resistance (R_s), a double layer capacitance (C_{dl}), an electron transfer resistance (R_{et}) and a Warburg impedance (Z_W). In these plots, the diameter of a semicircle in the high frequency region is related to R_{et} of $[Fe(CN)_6]^{3-}$/$[Fe(CN)_6]^{4-}$ at the corresponding electrode. A comparison between an experimental Nyquist plot and a simulated Nyquist plot based on the equivalent circuit will then yield a corresponding set of results for its elements. For convenience, we have tabulated the results obtained in the bottom inset of Fig. 4B. In our work, only results with a 99% agreement in the comparison were accepted as valid results. In this way, the Nyquist plot of $[Fe(CN)_6]^{3-}$/$[Fe(CN)_6]^{4-}$ at the TiO_2|glassy carbon electrode in trace a shows a large semicircle in the high frequency region, probably due to the poor electron transfer capacity of TiO_2. The R_{et} from the Nyquist plot at the Pt–Sn@TiO_2 modified electrode in trace b is 30% smaller than that at TiO_2, most likely attributed to the excellent electronic conductivity of Pt–Sn alloy nanoparticles. However, as shown in trace c and trace d, the larger R_{et} after successive modification with cDNA and BSA, and streptomycin aptamer, which resulted from the strong steric hindrance and insulation effect of proteins on $[Fe(CN)_6]^{3-}$/$[Fe(CN)_6]^{4-}$. In summary, these results provided supporting evidence that the materials were successively immobilised on the electrode surface.

To verify the assembly process of the designed electrochemical aptasensor and its feasibility for streptomycin detection, differential pulse voltammetry of saturated O_2 at successively modified electrodes was also conducted in 0.1 M PBS (pH 7.4) and the results obtained are displayed in Fig. 4C. As shown by trace a, a relatively weak peak current (~7.0 µA) was obtained at the TiO_2|glassy carbon electrode due to metal oxide semiconductor property and little catalytic activity of TiO_2. On the contrary, the corresponding peak current in trace b was ~33% larger at the Pt–Sn@TiO_2|glassy carbon electrode, attributed to the oxygen reduction reaction catalytic performance and good conductivity of Pt-based bimetal catalyst. After immobilising the DNA with a complementary sequence to the streptomycin aptamer and then BSA on the Pt–Sn@TiO_2|glassy carbon electrode, the peak current in trace c (~5.7 µA) was noticeably decreased by ~39%. Likewise, streptomycin aptamers were also immobilised on the electrode surface via DNA hybridisation, and the peak current in trace d (~4.5 µA) was diminished by ~52%, owing to the strong steric hindrance and electrostatic repulsive effect. Specifically, the negatively charged phosphate groups of DNA molecules strongly repel electrons, giving rise to an electrostatic repulsive effect that severely inhibited the electron transfer in oxygen reduction reaction progress, leading to a decrease of the current response. Finally, the aptasensor was incubated in 5 µL of 1.5 µM streptomycin and 20 U $RecJ_f$ exonuclease, the peak current in trace e dramatically re-grew to ~8.3 µA. This is because the specific binding of streptomycin aptamer with streptomycin caused the separation of the aptamer from cDNA to produce two single-stranded structures. $RecJ_f$ exonuclease then cleaved between the single strand aptamer and cDNA, resulting in the release of streptomycin for cyclic amplification and removed cDNA from the electrode. After multiple cleavage cycles, the number of biomolecules on the electrode surface decreased significantly and the charge transfer in oxygen reduction reaction was maximumly enhanced, causing evidently recovered differential pulse voltammetric peak current. In summary, differential pulse voltammetric characterisation demonstrated the successful construction of the aptasensor.

3.6. Optimisation of the electrochemical aptasensor

The concentration of $RecJ_f$ exonuclease and the enzymatic reaction time are both expected to strongly affect the performance of the aptasensor, and they were thus optimised based on the differential pulse voltammetric response of O_2-saturated 0.1 M PBS (pH 7.4). As illustrated by trace a in Fig. 4D, the oxygen reduction peak current increased as a function of $RecJ_f$ exonuclease concentration from 0 U to 30 U. However, at $RecJ_f$ exonuclease concentration higher than 20 U, there was no significant further increase in the oxygen reduction peak current, probably due to a saturated concentration of $RecJ_f$ exonuclease on the electrode surface. Accordingly, a $RecJ_f$ exonuclease concentration of 20 U was adopted as the optimum concentration for further experiments. Trace b shows the differential pulse voltammetric reduction of oxygen when the incubation time was extended from 0 h to 3 h. No significant increase in the peak current was observed when the incubation time was longer than 1.5 h. Accordingly, 1.5 h was used as the optimum enzymatic reaction time in the subsequent assays.

3.7. Electrochemical detection of streptomycin

Under the optimised conditions of 20 U $RecJ_f$ exonuclease and 1.5 h incubation time, the electrochemical aptasensor was employed for the quantitative determination of streptomycin. The electrochemical response of the fabricated streptomycin aptasensor in O_2-saturated solution was recorded. As shown in Fig. 5A, the differential pulse voltammetric signal increased with the increasing streptomycin concentration from 0 to 2000 nM. The background current-subtracted signal ($\Delta I = I - I_0$, where I_0 represents the blank differential pulse voltammetric peak current) in the inset of Fig. 5A is linearly related to the concentration of streptomycin ($C_{streptomycin}$) over the 0.05–1500 nM range. However, when $C_{streptomycin}$ exceeded 1500 nM, ΔI began to deviate from the linear range. The regression equation is determined as $\Delta I / \mu A = 2.32 \pm 0.017 / \mu A\, \mu M^{-1} \times C / \mu M + 0.0856 \pm 0.0092 / \mu A$ (all errors represent the 95% confidence intervals) with a correlation coefficient of 0.9953 ($N = 6$), which was found to be statistically significant at the 95% confidence level using Student's *t*-test. In addition, the result of a Wald-Wolfowit runs test has confirmed a random distribution of residuals in the corresponding residual plot, supporting a linear calibration plot. A detection limit based on a signal-to-noise ratio of 3 was estimated to be 0.020 nM ± 0.0045 nM (the error here again denotes the 95% confidence interval). Compared with several other reported methods for the detection of streptomycin tabulated in Table 1, the proposed electrochemical aptasensor exhibited a wider linear range and a lower detection limit. The excellent performance of the apatsensor was attributed to the large specific surface, high conductivity, good biocompatibility and pronounced oxygen reduction catalytic property of Pt–Sn@TiO_2 composite.

3.8. Stability, reproducibility and specificity of the electrochemical aptasensor

Selectivity is another important parameter for an aptasensor, which was investigated by comparing the differential pulse voltammetric response of 1.5 nM streptomycin to that of several antibiotics including streptomycin, chloramphenicol, erythromycin, kanamycin and ciprofloxacin at the same concentration. As shown in Fig. 5B, the target streptomycin exhibited an at least 16-fold higher ΔI relative to the other antibiotic interferents. We have attributed this to the specific interaction between the aptamer and streptomycin, indicating the high specificity of the aptasensor to streptomycin. The stability of the streptomycin aptasensor was further studied after aptasensors were stored at 4°C before measurement. The result showed that 90.7% of the initial differential pulse voltammetric peak current response retained after 7 days of storage, which demonstrated the good long-term stability of the aptasensor. Reproducibility is an important consideration for evaluating the performance of the aptasensor. To assess the reproducibility of the fabricated aptasensor, five identical aptasensors were used to determine streptomycin in the same experimental conditions. A relative standard deviation of 4.7% was obtained, indicating an excellent analytical reproducibility of the aptasensor. These results supported the feasibility of this aptasensor for sensitive streptomycin assays.

3.9. Application of the aptasensor to milk sample analysis

The practical application of the aptasensor was evaluated by determining different concentrations of streptomycin in milk samples. The milk samples obtained from a local supermarket were firstly centrifuged at 2000 rpm for 30 min. The supernatant was then collected and diluted 10-fold in PBS. Increasing quantity of streptomycin was added to the diluted milk samples to obtain the final concentration of 10, 70, 150, 300 nM. Finally, recovery experiments were performed by standard addition method in spiked milk samples. As shown in Table 2, recoveries ranging from 91.3% to 97.7% were estimated, which demonstrated the successful application of the proposed aptasensor for detection of streptomycin in real-life samples.

4. Conclusion

In summary, a highly sensitive and selective electrochemical aptasensor to streptomycin was developed incorporating a dual signal amplification system, which includes an oxygen reduction catalyst,

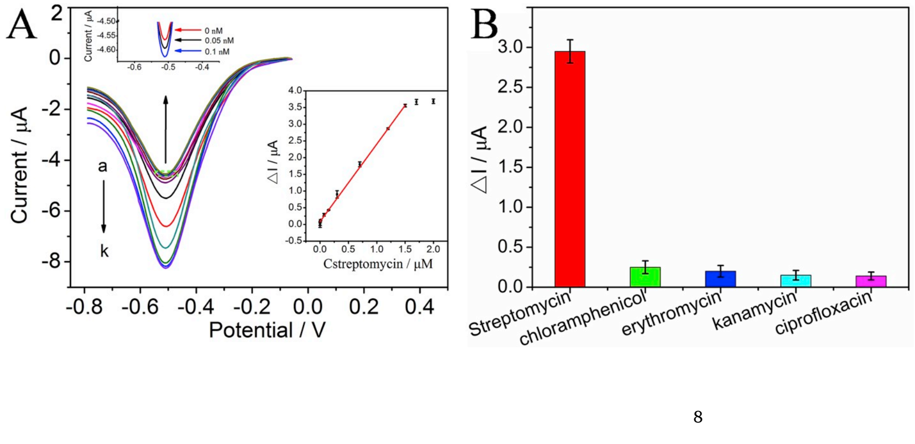

Fig. 5. (A) Differential pulse voltammetric response of different streptomycin concentration $(C)_{streptomycin}$; from a to i: 0, 0.05, 1, 10, 70, 150, 300, 750, 1200, 1500, 1700 and 2000 nM at the aptasensor in O_2-saturated 0.1 M PBS (pH 7.4). Inset: a plot of differential pulse voltammetric peak current change (ΔI) versus $C_{streptomycin}$; (B) Anti-interference property of the aptasensor in O_2-saturated 0.1 M PBS (pH 7.4) containing 1.5 nM streptomycin, chloramphenicol, erythromycin, kanamycin and ciprofloxacin containing 20 U $RecJ_f$ exonuclease. Error bars represent the standard deviations of measurements taken from four independent experiments.

Table 1
Comparison of analytical performance of different techniques for streptomycin detection.

Analytical technique	Linear range	Detection limit	References
Fluorescence	Not reported	54.0 nM	Taghdisi et al. (2016)
Colorimetry	0.20–12.0 μM	Not reported	Zhou et al. (2013)
Flow injection analysis-electrochemical quartz crystal nanobalance	0.51–85.0 nM	0.51 nM	Mishra et al. (2015)
Photoelectrochemical detection	0.10–50.0 nM	33.0 pM	Xu et al. (2017)
Differential pulse voltammetry	30–1500 nM	11.4 nM	Mohammad Danesh et al. (2016)
Differential pulse voltammetry	85.0–343 nM	48.0 pM	Yin et al. (2017)
Chemiluminescence	13.7–1710 nM	3.80 nM	Du et al. (2013)
Differential pulse voltammetry	0.05–1500 nM	0.02 nM	This work

Table 2
Determination of streptomycin in milk samples with the developed aptasensor (N = 3).

Samples	Added / nM	Found / nM[a]	Recovery / %	Standard deviation / nM
1	10	9.21 ± 0.02	92.1	0.087
2	70	67.5 ± 0.08	96.4	0.091
3	150	137 ± 0.1	91.3	0.102
4	300	293 ± 0.2	97.7	0.163

[a] All uncertainties represent the 95% confidence intervals.

Pt–Sn@TiO$_2$ composite, and an exonuclease assisted target recycling. The cylinder-shaped Pt–Sn@TiO$_2$ ternary composite exhibited a large specific surface to load biomolecules and excellent electrocatalytic activity towards oxygen reduction reaction, which considerably amplified the detection signal. Specifically, DNA hybridisation between streptomycin aptamer and cDNA on the electrode resulted in a relatively low peak current for oxygen reduction. The introduction of streptomycin and RecJ$_f$ exonuclease initiated a cyclic amplification mechanism and removed both streptomycin aptamer and cDNA from the electrode, leading to a 0.85-fold enhancement of the oxygen reduction peak current. A linear range of 0.05–1500 nM and a detection limit of 0.020 ± 0.0045 nM for streptomycin was obtained based on the above amplification mechanism. Moreover, the proposed electrochemical aptasensor exhibited 91.3%–97.7% reproducibility as well as good feasibility for real-life sample detection. This proposed strategy contributed to the design of highly efficient Pt-based bimetallic electrocatalysts with excellent oxygen reduction reaction catalytic property, which will show many potential applications in bioanalysis.

Declaration of competing interest

The authors declare that they have no known competing financial interests or personal relationships that could have appeared to influence the work reported in this paper.

CRediT authorship contribution statement

LeLe Li: Conceptualization, Methodology, Investigation, Funding acquisition, Writing - original draft, Software. **Xiaoqiang Liu:** Conceptualization, Methodology, Funding acquisition, Writing - original draft. **Liwei Yang:** Visualization. **Si Zhang:** Supervision. **HeJie Zheng:** Software. **Yunfei Tang:** Validation. **Danny K.Y. Wong:** Methodology, Writing - review & editing, Supervision.

Acknowledgements

This work was financially supported by National Natural Science Projects of China (No. U1504215, 21576071, 21776061), funded by Chinese National Natural Science Foundation; International Science and Technology Cooperation Project (172102410042), funded by Department of Science and Technology of Henan Province, China; the project for Science & Technology Innovation Talents in Universities of Henan Province (19HASTIT037) and the project for Science & Technology Innovation Team in Universities of Henan Province (19IRTSTHN029), both funded by Education Department of Henan Province.

References

Antolini, E., Salgado, J.R.C., Gonzalez, E.R., 2006. J. Power Sources 160, 957–968.
Bai, L., Yuan, R., Chai, Y., Yuan, Y., Zhuo, Y., Mao, L., 2011. Biosens. Bioelectron. 26, 4331–4336.
Beiranvand, Z.S., Abbasi, A.R., Dehdashtian, S., Karimi, Z., Azadbakht, A., 2017. Anal. Biochem. 518, 35–45.
Beyhan, S., Şahin, N.E., Pronier, S., Léger, J.-M., Kadırgan, F., 2015. Electrochim. Acta 151, 565–573.
Cao, J.-T., Zhang, J.-J., Gong, Y., Ruan, X.-J., Liu, Y.-M., Chen, Y.-H., Ren, S.-W., 2015. J. Electroanal. Chem. 759, 46–50.
Chen, J., Fan, G.-C., Shi, X.-M., Zhu, J.-J., 2017. ChemElectroChem 4, 927–934.
Chen, L., Sha, L., Qiu, Y., Wang, G., Jiang, H., Zhang, X., 2015. Nanoscale 7, 3300–3308.
Chen, M., Gan, N., Zhou, Y., Li, T., Xu, Q., Cao, Y., Chen, Y., 2016. Talanta 161, 867–874.
Chen, W., Yan, C., Cheng, L., Yao, L., Xue, F., Xu, J., 2018. Biosens. Bioelectron. 117, 845–851.
Cho, Y.-H., Kim, O.-H., Chung, D.Y., Choe, H., Cho, Y.-H., Sung, Y.-E., 2014. Appl. Catal. B Environ. 154–155, 309–315.
Deng, D., Hao, Y., Yang, S., Han, Q., Liu, L., Xiang, Y., Tu, F., Xia, N., 2019. Sens. Actuators, B 286, 415–420.
Dong, Y.-X., Cao, J.-T., Wang, B., Ma, S.-H., Liu, Y.-M., 2017. ACS Sustain. Chem. Eng. 5, 10840–10848.
Du, B., Li, H., Jin, J., Wang, T., Li, Y., Shen, G., Li, X., 2013. Spectrochim. Acta, Part A 115, 823–828.
Evtugyn, G.A., Stepanova, V.B., Porfireva, A.V., Zamaleeva, A.I., Fakhrullin, R.R., 2014. J. Nanosci. Nanotechnol. 14, 6738–6747.
Ghanbari, K., Roushani, M., 2018. Bioelectrochemistry 120, 43–48.
Golub, E., Pelossof, G., Freeman, R., Zhang, H., Willner, I., 2009. Anal. Chem. 81, 9291–9298.
Huo, X., Liu, P., Zhu, J., Liu, X., Ju, H., 2016. Biosens. Bioelectron. 85, 698–706.
Khotseng, L., Bangisa, A., Modibedi, R.M., Linkov, V., 2016. Electrocatalysis 7, 1–12.
Liu, P.P., Liu, X., Huo, X.H., Tang, Y., Xu, J., Ju, H., 2017a. ACS Appl. Mater. Interfaces 9, 27185–27192.
Liu, X., Huo, X., Liu, P., Tang, Y., Xu, J., Ju, H., 2017b. Biosens. Bioelectron. 92, 171–178.
Liu, X., Huo, X., Liu, P., Tang, Y., Xu, J., Liu, X., Zhou, Y., 2017c. Electrochim. Acta 242, 327–336.
Liu, X., Liu, P., Tang, Y., Yang, L., Li, L., Qi, Z., Li, D., Wong, D.K.Y., 2018. Biosens. Bioelectron. 112, 193–201.
Liu, X., Wang, W., Li, H., Li, L., Zhou, G., Yu, R., Wang, D., Li, Y., 2013. Sci. Rep. 3, 1404.
Maass, S., Finsterwalder, F., Frank, G., Hartmann, R., Merten, C., 2008. J. Power Sources 176, 444–451.
Miao, Y.-B., Ren, H.-X., Gan, N., Zhou, Y., Cao, Y., Li, T., Chen, Y., 2016. Biosens. Bioelectron. 86, 477–483.
Mishra, G.K., Sharma, A., Bhand, S., 2015. Biosens. Bioelectron. 67, 532–539.
Mohammad Danesh, N., Ramezani, M., Sarreshtehdar Emrani, A., Abnous, K., Taghdisi, S.M., 2016. Biosens. Bioelectron. 75, 123–128.
Ozdokur, K.V., Demir, B., Atman, E., Tatli, A.Y., Yilmaz, B., Demirkol, D.O., Kocak, S., Timur, S., Ertas, F.N., 2016. Sens. Actuators, B 237, 291–297.
Sai-Anand, G., Sivanesan, A., Benzigar, M.R., Singh, G., Gopalan, A.-I., Baskar, A.V., Ilbeygi, H., Ramadass, K., Kambala, V., Vinu, A., 2018. Bull. Chem. Soc. Jpn. 92, 216–244.
Sui, S., Wang, X., Zhou, X., Su, Y., Riffat, S., Liu, C.-j., 2017. J. Mater. Chem. 5, 1808–1825.
Taghdisi, S.M., Danesh, N.M., Nameghi, M.A., Ramezani, M., Abnous, K., 2016. Food Chem. 203, 145–149.
Tang, Y., Chai, Y., Liu, X., Li, L., Yang, L., Liu, P., Zhou, Y., Ju, H., Cheng, Y., 2018a. Biosens. Bioelectron. 117, 224–231.
Tang, Y., Liu, P., Xu, J., Li, L., Yang, L., Liu, X., Liu, S., Zhou, Y., 2018b. Sens. Actuators, B 258, 906–912.
Tavakkoli, N., Soltani, N., Mohammadi, F., 2019. RSC Adv. 9, 14296–14301.
Urbanová, V., Jayaramulu, K., Schneemann, A., Kment, Š., Fischer, R.A., Zbořil, R., 2018. ACS Appl. Mater. Interfaces 10, 41089–41097.

Wang, D., Lu, S., Jiang, S.P., 2010. Electrochim. Acta 55, 2964–2971.
Wang, L., Holewinski, A., Wang, C., 2018a. ACS Catal. 8, 9388–9398.
Wang, S., Xu, J., Ding, H., Pan, S., Zhang, Y., Li, G., 2012. CrystEngComm 14, 7672–7679.
Wang, X., Gao, W., Yan, W., Li, P., Zou, H., Wei, Z., Guan, W., Ma, Y., Wu, S., Yu, Y., Ding, K., 2018b. ACS Appl. Nano Mater. 1, 2341–2346.
Xu, X., Liu, D., Luo, L., Li, L., Wang, K., You, T., 2017. Sens. Actuators, B 251, 564–571.
Yang, Y., Yang, Z., Lv, J., Yuan, R., Chai, Y., 2017. Talanta 169, 44–49.
Yang, Z., Jian, Z., Chen, X., Li, J., Qin, P., Zhao, J., Jiao, X.a., Hu, X., 2015. Biosens. Bioelectron. 63, 190–195.
Yin, J., Guo, W., Qin, X., Zhao, J., Pei, M., Ding, F., 2017. Sens. Actuators, B 241, 151–159.
Zhang, E., Ma, F., Liu, J., Sun, J., Chen, W., Rong, H., Zhu, X., Liu, J., Xu, M., Zhuang, Z., Chen, S., Wen, Z., Zhang, J., 2018. Nanoscale 10, 21703–21711.
Zhang, K., Dong, H., Dai, W., Meng, X., Lu, H., Wu, T., Zhang, X., 2017. Anal. Chem. 89, 648–655.
Zhao, Z., Zhang, X., Zhang, G., Liu, Z., Qu, D., Miao, X., Feng, P., Sun, Z., 2015. Nano Res 8, 4061–4071.
Zheng, T., Zhang, Q., Feng, S., Zhu, J.-J., Wang, Q., Wang, H., 2014. J. Am. Chem. Soc. 136, 2288–2291.
Zhou, N., Wang, J., Zhang, J., Li, C., Tian, Y., Wang, J., 2013. Talanta 108, 109–116.